

# **Autonomous process set-up with Bayesian optimization for high shape fidelity in hydrogel-based 3D printing**

**Kyung-Lim Oh<sup>1</sup>, Suk-Hee Park<sup>1\*</sup>**

*<sup>1</sup> School of Mechanical Engineering, Pusan National University, Busan 46241, Republic of Korea*

\*To whom correspondence should be addressed.

Tel: +82-51-510-2894; Fax: +82-51-510-1973; E-mail: [selome815@pusan.ac.kr](mailto:selome815@pusan.ac.kr); ORCID: 0000-0002-5515-8660

### **Authorship contributions**

**Kyung-Lim Oh:** Conceptualization, Methodology, Investigation, Software, Validation, Visualization, Data curation, Writing – original draft, Writing – review & editing. **Suk-Hee Park:** Supervision, Conceptualization, Methodology, Funding acquisition, Writing – review & editing.

### **Acknowledgments**

This work was supported by the National Research Foundation of the Korea (NRF) grant funded by Korea government (MSIT) (No. RS-2023-00213269).

### **Declarations**

### **Competing interests**

The authors declare no competing interests.

### **Data Availability Statement**

The datasets generated during this study are not publicly available but are available from the corresponding author upon reasonable request.

## **Abstract**

In extrusion-based 3D printing, particularly with challenging materials, optimizing printing parameters is crucial for improving print quality. Hydrogels, characterized by viscoelasticity and shear-thinning behavior, present significant challenges in extrusion control. To address these challenges, this study proposes a Bayesian optimization (BO) framework to autonomously optimize printing parameters—pre-loading, nozzle movement speed, and extrusion rate—and improve process efficiency with print stability. Due to the complexity of the extrusion process, experimental data were used instead of physical models or simulations. Preliminary experiments identified key defects such as infill void and tail leakage, which were quantified using image preprocessing and custom scoring methods. BO was applied to iteratively refine printing parameters through an autonomous setup, enabling rapid convergence toward the optimal settings. The system efficiently optimized parameters within 10 iterations across different sizes, shapes, and material concentrations. Furthermore, the optimized in-plane parameters were successfully extended to 3D structures using a layer-by-layer deposition approach. This framework provides a robust and efficient solution for improving the print quality in complex materials like hydrogels, ensuring high precision and overall process stability in extrusion-based 3D printing.

**Keywords:** Extrusion-based 3D printing; Hydrogel printing; Bayesian optimization; Printing parameter optimization

## Introduction

Additive manufacturing is an innovative technology that enables the rapid fabrication of complex geometries through layer-by-layer construction based on CAD modeling (He et al., 2019). It supports a diverse range of materials, including metals, polymers, and ceramics (Bourell et al., 2017), allowing for the development of customized solutions tailored to specific requirements (Huang et al., 2015). Consequently, additive manufacturing has been widely adopted across various industries and continues to demonstrate transformative potential, particularly in multi-variety customized production (Kumar et al., 2023). However, persistent challenges such as delamination (Siegel et al., 2020), distortion (Saluja et al., 2020), extrusion defects (He et al., 2024), and rough surfaces (Whip et al., 2019) degrade the quality of manufactured components. These limitations hinder the broader application of additive manufacturing, highlighting the need for precise technical evaluation and process optimization to improve reliability and performance.

Extrusion-based 3D printing is a widely used method in additive manufacturing due to its straightforward mechanism and ease of implementation (Jiang et al., 2020). It accommodates a broad spectrum of materials from high-viscosity options like super-engineering plastics and ceramic slurries to low-viscosity materials such as hydrogels and polymer solutions (Saadi et al., 2022). Among these, hydrogel is a particularly versatile material due to its softness and high water absorbency, making it well-suited for applications in bioprinting (Li et al., 2016), drug delivery (Munoz-Perez et al., 2024), and food printing (Umeda et al., 2024). However, managing it poses significant challenges due to its viscoelasticity and shear-thinning behavior, which often lead to material spreading and deformation, compromising shape fidelity (Yang et al., 2023). The process is further complicated by interactions among variables such as temperature, humidity, nozzle size, and print speed, making it difficult to predict extrusion behavior accurately (Naghieh et al., 2019). Since defects that occur during printing are difficult to correct due to the complexity between material properties and extrusion dynamics, prior optimization of printing parameters is essential for achieving high shape fidelity (Zheng et al., 2023). Recent research has focused on enhancing additive manufacturing quality by moving beyond traditional trial-and-error methods (Armstrong et al., 2021; Webb & Doyle, 2017), where printing parameters are manually adjusted, toward advanced optimization techniques utilizing artificial intelligence (AI) and machine learning (ML) to streamline process control.

AI- and ML-based approaches are increasingly recognized for their potential to enhance additive manufacturing quality. These methods are typically applied in two main ways: real-time process monitoring and pre-optimization. In real-time monitoring, sensor-based data (Shevchik et al., 2019) and vision-based data (Franke et al., 2024) are used to detect abnormal changes during printing, allowing for immediate adjustments to prevent defects (Lee & Park, 2025). However, in certain printing processes, defects are difficult to correct after detection due to material properties or complex interactions between process parameters (Zheng et al., 2023). As a result, real-time monitoring alone may not be sufficient to ensure high-quality outcomes. In such cases, a pre-optimization phase is essential, where printing or design parameters (Dharmadhikari et al., 2023; Qin et al., 2019) are fine-tuned to minimize the risk of defects. Algorithmic ML optimization methods, such as Bayesian optimization (BO) and genetic algorithms (Jung et al., 2023; Sridhar et al., 2024; Vaissier et al., 2019), utilize existing data or simulations to efficiently explore the parameter space and identify optimal settings while reducing reliance on labor-intensive trial-and-error experiments. This approach significantly improves process efficiency by minimizing the need for extensive experimental iterations. Among these methods, BO stands out for its ability to quickly identify optimal solutions with minimal data, making it particularly valuable when data collection is costly or time-consuming (Frazier, 2018). BO uses a surrogate model based on Gaussian Process Regression (GPR), which predicts outcomes while incorporating uncertainty into these predictions. This probabilistic approach enables BO to balance exploration of new regions with exploitation of promising areas, making the most efficient use of available data. BO is widely employed in hyperparameter tuning, particularly when the objective function is unknown or treated as a black-box function. It has proven effective in various manufacturing applications, such as reducing computational costs in simulation-based studies and identifying optimal material combinations with limited data (Zhang et al., 2020). In the context of additive manufacturing, BO has further demonstrated its effectiveness by reducing the number of experiments required to achieve optimal process conditions (Chepiga et al., 2023; Liu et al., 2022).

In this study, we propose a novel framework for autonomously optimizing printing parameters in extrusion-based 3D printing of hydrogels using BO. The framework addresses the challenges posed by the viscoelastic and shear-thinning properties of hydrogels, which often lead to shape deformation and defects during printing. By utilizing experimental data instead of complex physical simulations, the proposed method identifies and quantifies key defects such as infill void and tail leakage through image preprocessing and scoring techniques. Each defect is modeled with

a separate Gaussian Process Regression (GPR) model, and the predicted outputs are combined into a single objective function for optimization. BO is then applied iteratively in an automated closed loop to refine the printing parameters, ensuring optimal quality with minimal iterations. Furthermore, the study extends the optimized in-plane parameters to 3D structures, enabling stable layer-by-layer deposition for hydrogel materials. This autonomous approach not only simplifies the parameter optimization process but also highlights the potential of BO to enhance additive manufacturing quality for challenging materials. By improving print stability and precision, this framework broadens the applicability of hydrogel printing to areas such as bioprinting, drug delivery, and advanced fabrication with functional materials.

## **Materials and methods**

### **Extrusion-based printing system**

The hydrogel-based 3D printing system was implemented by modifying a commercial 3D printer (Ender 3 V2, Creality, China). The original filament-based extruder was removed and replaced with a stepper motor-driven syringe pump to create a direct extrusion system (Appendix Fig. 9). To ensure stable lateral motion of the syringe pump, an additional belt was incorporated, allowing the pump to operate along two parallel belts. A custom metal plate was mounted to adjust the center of gravity, preventing pump tilting and ensuring consistent contact between the pump wheel and the belts. The syringe pump was controlled by connecting it to the motor control lines originally designated for filament feeding. A Raspberry Pi was integrated into the system to facilitate computer communication for printer control and data acquisition. The printing process was monitored and controlled via the OctoPrint web interface.

### **Materials**

Sodium alginate (SA, Aladdin, China) was selected for its simplicity and versatility as adjusting its concentration allowed for easy manipulation of viscosity to replicate different material properties. To prepare the solutions, the alginate was dissolved in deionized water at concentrations of 4% and 6%. Air bubbles were removed

from the solutions prior to use to ensure consistent extrusion characteristics. A red pigment was added to the transparent alginate to enhance contrast during image capture. Extrusion was performed using a 25G cutting needle.

### **Experimental data acquisition for machine learning**

Four preliminary experiments were conducted to collect data for optimization. Different geometries and material concentrations were selected to represent a range of printing conditions: a 10×10 mm square with 4% alginate, a 20×20 mm square with 4% alginate, a 10 mm diameter circle with 4% alginate, and a 10×10 mm square with 6% alginate. The printing parameters chosen for optimization were pre-loading, nozzle movement speed, and extrusion rate. Random combinations of these three parameters were used to generate G-code in MATLAB. For the square prints, extrusion involved a vertical back-and-forth motion to form an infill grid, followed by horizontal movements to complete the print. The nozzle then traced the outline, after which extrusion was stopped before moving to the predetermined termination point. For the circular prints, extrusion commenced at the center and followed concentric paths of increasing radius until reaching the target diameter, after which extrusion was stopped and the nozzle moved to the endpoint. The extrusion results were captured using a camera module (B0197, ArduCam, China). To maintain consistent imaging conditions regardless of nozzle movement, the camera was mounted on the syringe pump and positioned 60 mm from the nozzle tip. The captured images were subsequently processed to evaluate infill void and tail leakage, converting the visual data into numerical form for training machine learning models within the BO framework.

### **Bayesian optimization**

BO is an algorithm for identifying optimal parameters where an acquisition function selects promising candidates based on a surrogate model (Shahriari et al., 2015). In this study, the surrogate model was developed using Gaussian Process Regression (GPR) on a dataset comprising printing parameters and their corresponding quality scores obtained from preliminary experiments. Both the input (printing parameters) and output (quality scores) data from the preliminary experiments were standardized to ensure consistent scaling during model training. Separate GPR models were constructed for each output variable: the infill void score and the tail leakage score. We compared Spectral mixture (SM), Squared-exponential (SE), and Matern under identical evaluation (80/20 train-test split, three

repetitions). Dataset 1 consisted of 4% alginate with a 10×10 mm square and Dataset 2 used 6% alginate. *For Dataset 1, the RMSE (Root mean squared error) values (mean ± SD) were: infill void—SM 0.099 ± 0.009, SE 0.100 ± 0.024, Matern 0.105 ± 0.018; tail leakage—SM 0.185 ± 0.055, SE 0.214 ± 0.082, Matern 0.208 ± 0.086. For Dataset 2, the RMSE values were infill void—SM 0.105 ± 0.041, SE 0.121 ± 0.034, Matern 0.109 ± 0.037; tail leakage—SM 0.168 ± 0.035, SE 0.313 ± 0.092, Matern 0.295 ± 0.081.* Across both datasets and both targets, SM consistently achieved the lowest mean RMSE and was therefore selected. Conceptually, SE and Matern are single-scale kernels suited to smooth global trends, whereas SM combines multiple scales in a single model, capturing both broad trends and local variations (Wilson & Adams, 2013). Model training was performed over 50 iterations using the Adam (Adaptive moment estimation) optimization algorithm to iteratively adjust the model parameters. A learning rate of 0.1 was employed, and the Exact Marginal Log-Likelihood function was used as the loss function to optimize prediction accuracy. The objective function was defined as the sum of the absolute values of the predicted means from the two GPR models. For the acquisition function, the Probability of Improvement (PI) was applied with the exploration parameter ( $\xi$ ) set to 0.5 (Gan et al., 2021). PI selects the variables with the highest probability of improving the objective function during each BO iteration as described in Eq. (1):

$$PI(x) = \Phi\left(\frac{f_{min} - \mu(x) - \xi}{\sigma(x)}\right) \quad (1)$$

Where  $\Phi$  is the cumulative distribution function of a standard normal distribution,  $f_{min}$  is the current minimum of the objective function,  $\mu(x)$  is the predicted mean at point  $x$ ,  $\sigma(x)$  is the standard deviation, and  $\xi$  balances exploration and exploitation. A smaller value of  $\xi$  focuses the search around the best-known solution, while a larger value promotes exploration of less-sampled regions. BO was executed to minimize the objective function using the `gp_minimize` function with 80 iterations for each experiment. Initial search points were randomly selected with the number varied depending on the experimental case.

## Results and discussion

### Defect characterization and printing parameter settings

Defects such as infill void and tail leakage commonly occur during the extrusion process in hydrogel printing,



significantly affecting shape fidelity. Infill void typically results from extrusion delay or material shortage (Fig. 1a). Extrusion delay occurs when the available pressure is insufficient to initiate material flow, and this is influenced by the pressure drop in non-Newtonian fluids. In Newtonian fluids, Poiseuille's law describes how pressure drop increases as viscosity rises or nozzle diameter decreases. However, for shear-thinning materials, viscosity decreases under shear, requiring an extended model. The Herschel-Bulkley equation incorporates both the material's yield stress and shear-dependent viscosity, describing the pressure drop relationship in Eq. (2) (Amorim et al., 2021; Rau et al., 2023):

$$\Delta P = \frac{2L}{R} (\tau_0 + k(\dot{\gamma})^n) \quad (2)$$

where  $\Delta P$  is the pressure drop,  $L$  is the nozzle length, and  $R$  is the nozzle radius. The parameters  $\tau_0$  (yield stress) and  $k$  (consistency index) characterize the material's resistance to flow, while  $n$  (flow behavior index,  $0 < n < 1$ ) describes the shear-thinning effects. According to this model, a smaller nozzle or a more viscous material increases pressure drop, requiring higher initial pressure for extrusion. Materials with high yield stress require pre-loading to overcome resistance, and insufficient pressure can lead to extrusion delay (Armstrong et al., 2020). Additionally, if the extrusion volume is too low relative to the nozzle movement speed, material shortage occurs, causing unstable deposition and thinner extruded lines, which contribute to void formation (He et al., 2016).

As shown in Fig. 1b, tail leakage is characterized by unintended flow of hydrogel material after printing is complete, which impairs overall shape fidelity. This defect is typically caused by residual internal pressure, which continues to drive material flow after extrusion ceases (Mantelli et al., 2021). Additionally, excessive material feeding can contribute to tail leakage when the extrusion volume is too high relative to the nozzle speed, leading to over-deposition (Jin et al., 2017). Fig. 1c and Fig. 1d show the printed results with infill void and tail leakage, respectively, emphasizing the need for effective mitigation strategies. To mitigate these issues, three key parameters for the printing process were identified as optimization targets: pre-loading, nozzle movement speed, and extrusion rate (Fig. 1e). Pre-loading is applied at the start of printing as a preliminary material loading step to pressurize the material inside the syringe, ensuring that the nozzle is properly filled before printing begins (Estelle & Gozen, 2022). This process prevents extrusion delay by overcoming the initial pressure drop required to immediately initiate material flow. Without pre-loading, insufficient pressure at the start can lead to unstable extrusion or void formation at the beginning

of the printed line. The extrusion rate (mL/s) represents the material dispensing rate per unit time during printing. The nozzle movement speed (mm/min) regulates the deposition rate on the substrate where excessively high speeds result in insufficient material deposition, while overly slow speeds may cause over-deposition and redundant material accumulation.

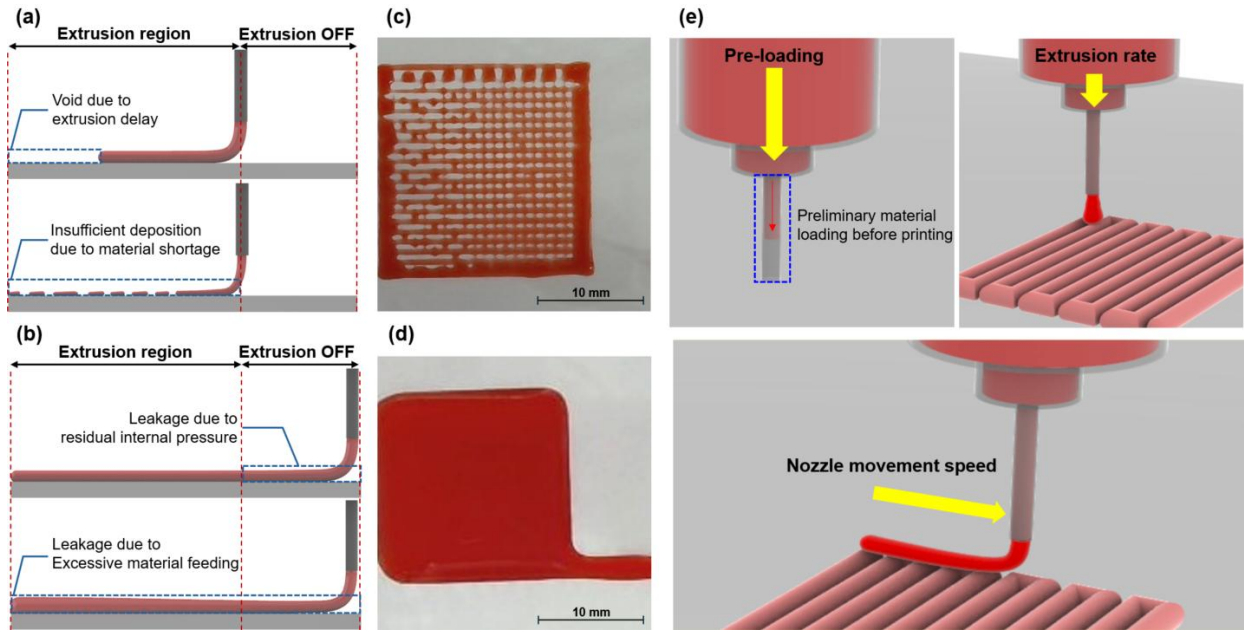


**Fig. 1** Defect characterization and printing parameter settings, **a** infill void caused by extrusion delay or material shortage, **b** tail leakage caused by residual internal pressure or excessive material feeding, **c** printed result showing infill void, **d** printed result showing tail leakage, **e** printing parameters targeted for optimization

### Quantification of quality scores from image data for machine learning

Infill void and tail leakage defects in printed results were evaluated using image preprocessing and a scoring method. As shown in Fig. 2a, images were acquired at a fixed focal length of 60 mm, and the capture position was defined in the G-code at a constant XY offset from the print start point to ensure a consistent view across all prints. All image preprocessing steps were implemented using the OpenCV library. As illustrated in Fig. 2b, images were

converted to grayscale, contrast-enhanced via CLAHE (clipLimit = 1.0, tile grid size = 1×1), and processed with a global threshold of 125 to generate a binary mask in which black pixels represented deposited material and white pixels indicated empty regions. One dilation (3 × 3 rectangular kernel) was then applied to this pre-inversion mask, followed by inversion so that deposits were white (255) and empty regions black (0). The choice of these parameters was supported by a one-variable-at-a-time analysis on representative tail leakage and infill void cases (Fig. 10). Tail leakage was largely insensitive to parameter changes, whereas void showed higher sensitivity. Increasing the CLAHE clipLimit to 1.5 over-enhanced background texture, while lowering it to 0.5 suppressed contrast and hid fine voids. Raising the threshold to 140 classified more mid-gray pixels as below the threshold (black). After bit inversion, those pixels became deposits (white), which shrink empty regions and underestimate voids. Lowering the threshold to 110 had the opposite effect, inflating void estimates. Increasing dilation to two iterations enlarged empty regions pre-inversion, leading to overestimation of voids after inversion, whereas zero iterations underestimated voids. Across both cases, the baseline settings (clipLimit = 1.0, threshold = 125, dilation = 1) consistently yielded the cleanest boundaries and the most reliable void segmentation.

Infill void defects were quantified by counting the number of black pixels inside the contour of the target shape (Fig. 2c), thereby providing a quantitative basis for evaluating infill void quality. The infill void score was defined as shown in Eq. (3):

$$\text{Infill void score} = \frac{\text{Black pixels}}{\text{Black pixels} + \text{White pixels}} \quad (3)$$

A score of 0 indicates the absence of black pixels, meaning that deposition was successful with no voids inside the target shape. Conversely, as the score approaches 1, it indicates an increase in voids within the target shape, caused by extrusion delays or material shortages. This scoring method, which calculates pixel ratios within the target shape contour, is applicable to shapes with any complexity and effectively captures internal defects.

Tail leakage defects were quantified by determining the bounding area, defined as the smallest rectangular contour encompassing the entire deposited region, and then comparing its size to that of the target shape (Eq. (4) and Fig. 2c).

$$\text{Tail leakage score} = \frac{|\text{Bounding area} - \text{Target area}|}{\text{Target area}} \quad (4)$$

For this analysis, only the outermost contour of the deposited region was extracted. The contour was simplified to remove small-scale serrations while preserving the overall geometry, and the smallest rectangular contour encompassing this contour was determined for area comparison with the target shape. A score of 0 indicates that the bounding contour area of deposited material matches the target shape area, indicating no leakage. As it increases, the bounding rectangular contour enlarges, resulting in a higher tail leakage score. Unlike the infill void score, which ranges from 0 to 1, the tail leakage score can exceed 1 if the bounding rectangle significantly expands, indicating severe leakage. This scoring system is designed so that lower scores correspond to higher printing quality. By extracting features based on contrast differences between the deposited object and its background, the method effectively quantifies defects without relying on complex techniques. This approach not only simplifies quality assessment across various shapes and processes but also facilitates efficient optimization.

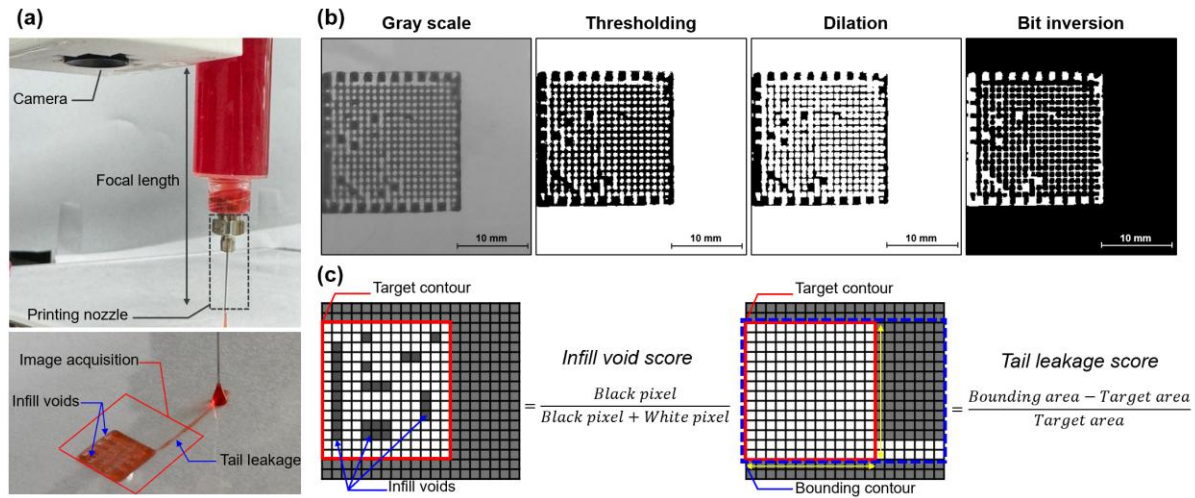


**Fig. 2** Data acquisition and quantification for machine learning, **a** image acquisition module equipped with the printing system, **b** preprocessing of acquired image data, **c** quantification of infill void and tail leakage scores

### Automated Bayesian optimization of multivariate printing parameters

The optimization process in this study follows the workflow illustrated in Fig. 3. It begins with data

collection from the preliminary experiment that serves as the foundation for constructing Gaussian Process Regression (GPR) models. Separate GPR models are built for the two defect types, infill void and tail leakage. As shown in Fig. 3a, each GPR model predicts the quality score corresponding to specific printing parameters, capturing the probabilistic relationship between printing parameters and quality score to provide insight into how printing conditions influence print quality. Next, as depicted in Fig. 3b, an objective function is defined as the sum of the absolute values of the predicted means from the two GPR models. This combined model enables simultaneous optimization of both defects, efficiently approximating the complex relationship between printing parameters and quality scores. Based on this model, the acquisition function identifies the next set of experimental parameters by evaluating the likelihood of quality improvement (Fig. 3c). Parameter search was conducted using the Probability of Improvement (PI) acquisition function with the hyperparameter  $\xi$  set to 0.5.  $\xi$  controls the balance between exploration and exploitation: small values bias the search toward regions near the current best, while larger values favor high-uncertainty regions (Lizotte, 2008). We compared  $\xi$  values of 0.1, 0.5, and 1.0 across random seeds. As shown in Fig. 11,  $\xi = 0.1$  led to rapid early improvement but plateaued due to over-exploitation, whereas  $\xi = 1.0$  progressed slowly because of excessive exploration.  $\xi = 0.5$  consistently achieved the lowest or near-lowest final objective values with steady improvement, indicating robust convergence behavior. Therefore,  $\xi = 0.5$  was adopted as the default in this study to ensure a stable and effective balance between exploration and exploitation.

The BO procedure was run for a fixed 80 iterations. Each recommended parameter set was automatically converted into G-code, tested in the printing process, and iteratively integrated into the dataset. This fully automated optimization cycle continued until the target quality scores—an infill void score of 0 and a tail leakage score of  $\leq 0.02$ —were achieved in physical experiments. These thresholds were selected because image preprocessing steps, such as contour detection and noise removal, introduce minor but unavoidable variations in leakage measurements. As illustrated in Fig. 3d, the optimization process involves iterative updates to the surrogate model. The acquisition function autonomously recommends the next parameter set based on the current surrogate model, reducing uncertainty in areas where the new data are incorporated. Once the corresponding quality scores are evaluated and added to the dataset, the surrogate model is updated, further refining its understanding of the relationship between printing parameters and quality scores. Through this automated optimization process, the model continuously improves its predictive capability, progressively converging toward optimal printing conditions. Although Fig. 3 presents an

optimization process focusing solely on nozzle movement speed while keeping pre-loading and extrusion rate fixed, the actual optimization is multivariate, simultaneously refining all three parameters. This approach ensures rapid convergence to optimal printing parameters, improving both process efficiency and print quality even in the presence of multivariate complexity.

As shown in Fig. 4a, Bayesian optimization for printing a 10×10 mm square was completed in six iterations. Iteration 1 used an extrusion rate of 0.014 mL/s and a nozzle movement speed of 883 mm/min, which led to severe tail leakage with a score of 1.75 due to over-deposition. By Iteration 3, the algorithm recommended a higher extrusion rate of 0.037 mL/s, but insufficient pre-loading caused delayed material extrusion, and the high nozzle movement speed exacerbated void formation. The final optimized parameters—0.55 mm pre-loading, 1298.4 mm/min nozzle speed, and 0.005 mL/s extrusion rate—achieved a well-balanced deposition, effectively minimizing both infill void and tail leakage. At this optimal point, the surrogate model predicted a mean quality score of 0.1042 with a corresponding 95% credible interval (CI) of [0.0992, 0.1092]. This indicates a high degree of confidence in the model's predictions and its ability to reliably recommend process parameters. Each iteration was executed autonomously from recommendation to evaluation. Fig. 4b and Fig. 4c provide additional insight into the interactions between pre-loading, nozzle movement speed, and extrusion rate involving their effects on print quality. As shown in Fig. 4b, higher pre-loading significantly reduced infill void formation by stabilizing initial extrusion and ensuring uniform material deposition. In contrast, the deposition quality was primarily dictated by the interaction between nozzle movement speed and extrusion rate. However, the maximum achievable extrusion rate was inherently limited by nozzle size and the distance between the nozzle and the print bed. Excessive nozzle speed relative to the extrusion rate led to void formation due to insufficient material deposition, whereas slower movement resulted in over-deposition by accumulating excess material. Fig. 4c highlights the trade-offs associated with nozzle speed. A higher nozzle speed mitigated tail leakage by rapidly moving the nozzle away, preventing excessive material deposition from distorting the shape. Conversely, a slower nozzle speed stabilized deposition but increased tail leakage due to prolonged contact at the endpoint of printing, where residual stress caused the extruded material to be more prone to unintended leakage.

This study demonstrates the effectiveness of BO in navigating a multivariate parameter space to simultaneously optimize pre-loading, nozzle movement speed, and extrusion rate while satisfying two critical quality

metrics. The optimization process successfully identified parameter sets that met both quality criteria, ensuring minimal infill void and tail leakage. Unlike conventional single-variable optimization approaches, this study addressed multivariate complexity by simultaneously optimizing three interdependent parameters. Furthermore, all optimization steps, from parameter recommendation to G-code generation and experimental validation, were performed autonomously within the BO framework. This emphasizes the robustness of BO for complex, multi-objective process optimization and its potential for broader applications in extrusion-based printing across diverse functional materials.

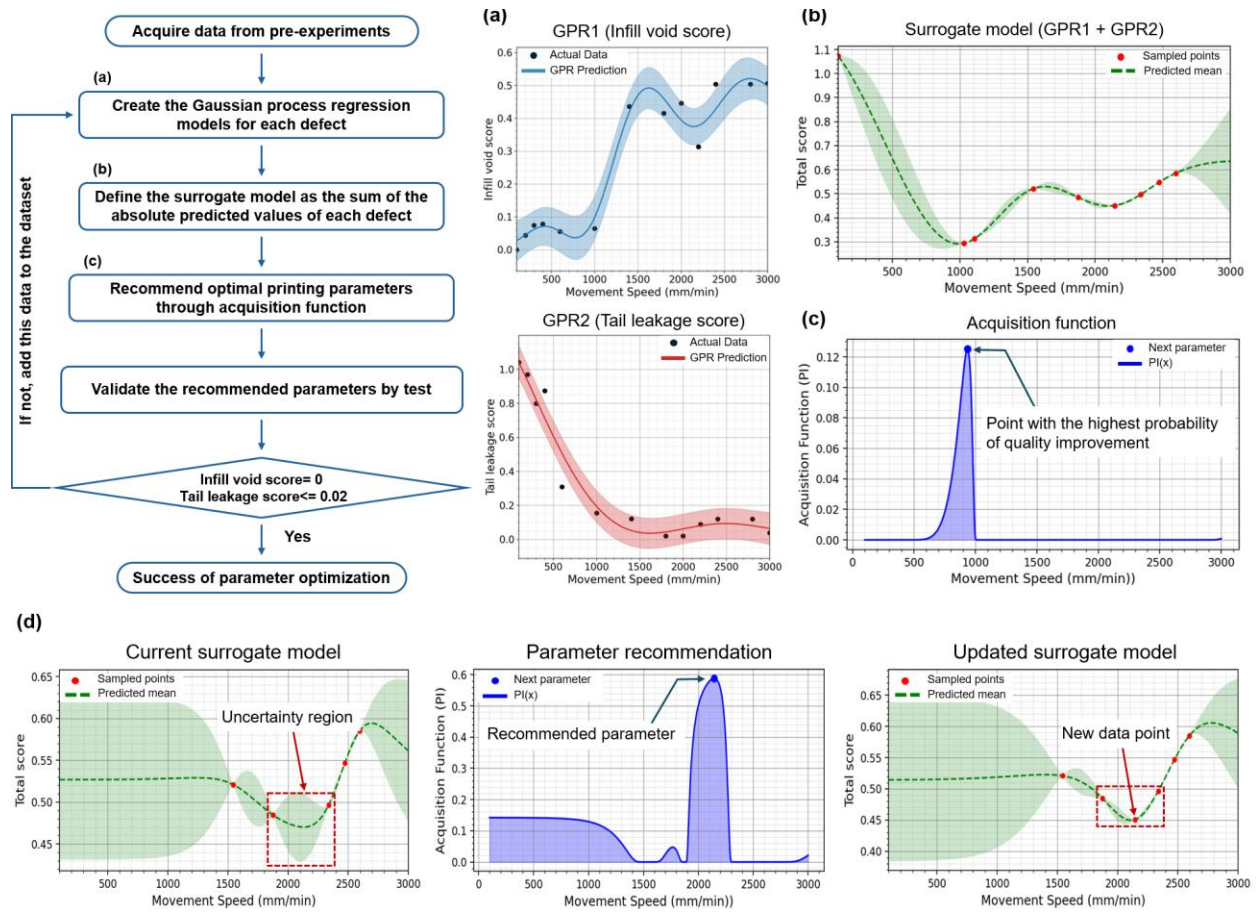


**Fig. 3** Workflow of Bayesian optimization, **a** GPR models for infill void (GPR1) and tail leakage (GPR2), **b** surrogate model constructed by combining both GPR models. The shaded areas indicate uncertainty, **c** acquisition function determining the next parameter set, **d** iterative refinement of the surrogate model through acquisition function-driven parameter recommendations



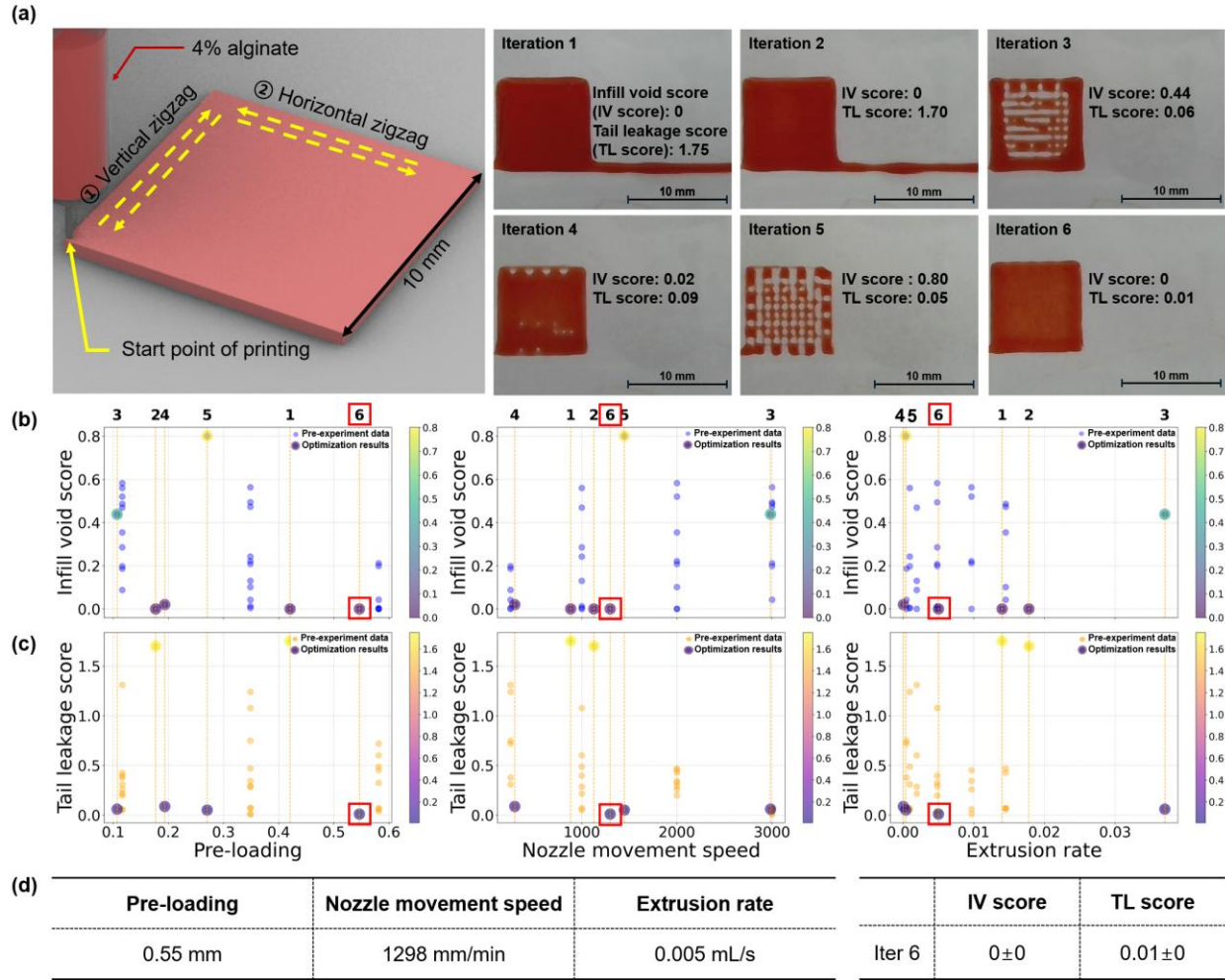


**Fig. 4** **a** Bayesian optimization process for 10×10 mm square with 4% alginate, **b** infill void and **c** tail leakage scores plotted against pre-loading, nozzle movement speed, and extrusion rate. Square markers indicate the optimized parameter set achieved at Iteration 6, **d** optimization results

#### Applicability of Bayesian optimization to different printing conditions

To assess its adaptability, the BO framework was tested under varying printing conditions, including a larger print size (20×20 mm), a different shape (circular path), and a higher material concentration (6% alginate). As shown in Fig. 5a, the 20×20 mm printing condition was optimized over six iterations. As the extrusion path length increased, the influence of pre-loading gradually diminished. Instead, nozzle movement speed and extrusion rate became the



dominant factors influencing overall print quality, as shown in Fig. 5b. Lower nozzle speeds consistently reduced infill void formation, but complete prevention of voids was achieved when the extrusion rate was also appropriately adjusted. Fig. 5c shows that tail leakage was minimal in the optimized parameter space, occurring only when extrusion rates were excessively high compared to nozzle speed, which led to over-deposition. The final optimized parameters—0.72 mm pre-loading, 1380 mm/min nozzle speed, and 0.004 mL/s extrusion rate—successfully minimized infill void while ensuring stable deposition. The predicted mean quality score at the optimum was 0.0561 (95% CI: [0.0462, 0.0659]).

For circular path printing (Fig. 6), optimization was completed in four iterations. The center region was primarily influenced by the initial extrusion force, while the outer regions were affected by nozzle movement speed and extrusion rate. However, excessive extrusion could lead to tail leakage, highlighting the importance of a well-balanced parameter combination. Fig. 6b shows that the lower initial extrusion resulted in a higher infill void score with Iteration 2 demonstrating void formation in the center due to insufficient initial extrusion. In contrast, extrusion rate and nozzle movement speed alone did not show a clear correlation with void formation. Fig. 6c reveals that tail leakage occurred across multiple parameter combinations, indicating that the selected parameter range included conditions prone to leakage. Both Iteration 1 and Iteration 3 exhibited leakage despite having different nozzle movement speeds (990 mm/min and 1684 mm/min). This suggests that the variation in nozzle movement speed within the given range was not sufficient relative to the extrusion rate to mitigate excessive deposition. The optimized result incorporated a high pre-loading of 0.61 mm to eliminate central voids, while a high nozzle movement speed of 2920.42 mm/min effectively redirected excess material from the initial extrusion, ensuring efficient material utilization and stable deposition. Additionally, the optimized low extrusion rate of 0.002 mL/s minimized tail leakage, confirming that this parameter combination produced the highest quality extrusion result. The predicted mean quality score at the optimum was 0.0337 (95% CI: [0.0308, 0.0367]).

The optimization of a 10×10 mm square with a 6% alginate concentration was achieved in eight iterations (Fig. 7a). The increased material concentration required a higher shear rate for stable initial extrusion. However, unlike with 4% alginate, higher pre-loading did not consistently reduce infill void formation. As shown in Fig. 7b, Iterations 5, 6, and 7 still exhibited voids despite high pre-loading, while in Iteration 4 a lower pre-loading setting combined with an increased deposition rate reduced voids but also led to leakage. Fig. 7b shows no clear trend between pre-

loading and infill void, suggesting that void formation is influenced by the combined effect of multiple parameters. In Fig. 7c, tail leakage was generally infrequent, although a slight increase in leakage frequency was observed at lower nozzle movement speeds. This phenomenon was attributed to the high viscosity of the solution where slower nozzle movement caused the solution to trail, leading to leakage as it failed to break off cleanly. BO recommended a pre-loading of 0.724 mm, a nozzle movement speed of 2479.1 mm/min, and an extrusion rate of 0.007 mL/s, achieving stable extrusion without infill void formation while preventing tail leakage through rapid nozzle movement. The predicted mean quality score at the optimum was 0.1482 (95% CI: [0.0670, 0.2290]). By autonomously adjusting parameters across different print sizes, shapes, and material concentrations, BO demonstrated its effectiveness in addressing diverse printing challenges. These findings confirm that BO is a robust and reliable method for systematically optimizing complex, multivariate extrusion processes.

For all four optimization cases, three independent prints were performed for each BO-recommended parameter set to evaluate reproducibility. The triplicate outcomes, including images of each repetition and the corresponding mean and standard deviation, were presented in Appendix Figs. 12-15 for the 10×10 mm square, 20×20 mm square, 10 mm circle, and the 10×10 mm square with 6% alginate. Variation across replicates was minimal in all cases, indicating that the optimized parameters consistently produced similar quality across independent fabrications. This analysis substantiates both the process-level reproducibility and the practical stability of the recommended printing parameters.

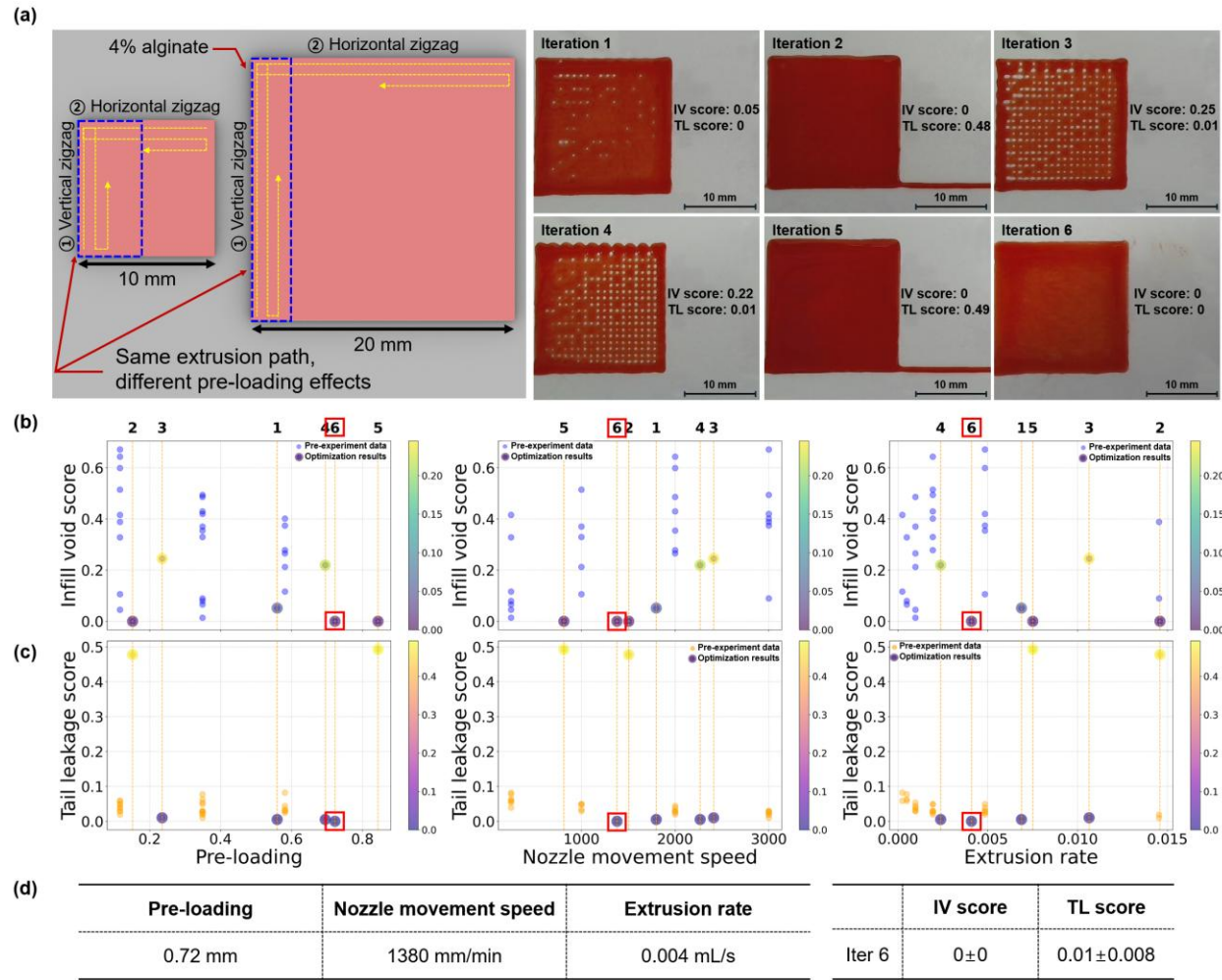


**Fig. 5** **a** Bayesian optimization process for 20×20 mm squares, **b** infill void and **c** tail leakage scores plotted against the pre-loading, nozzle movement speed, and extrusion rate. Square markers indicate the optimized parameter set achieved at Iteration 6, **d** optimization results

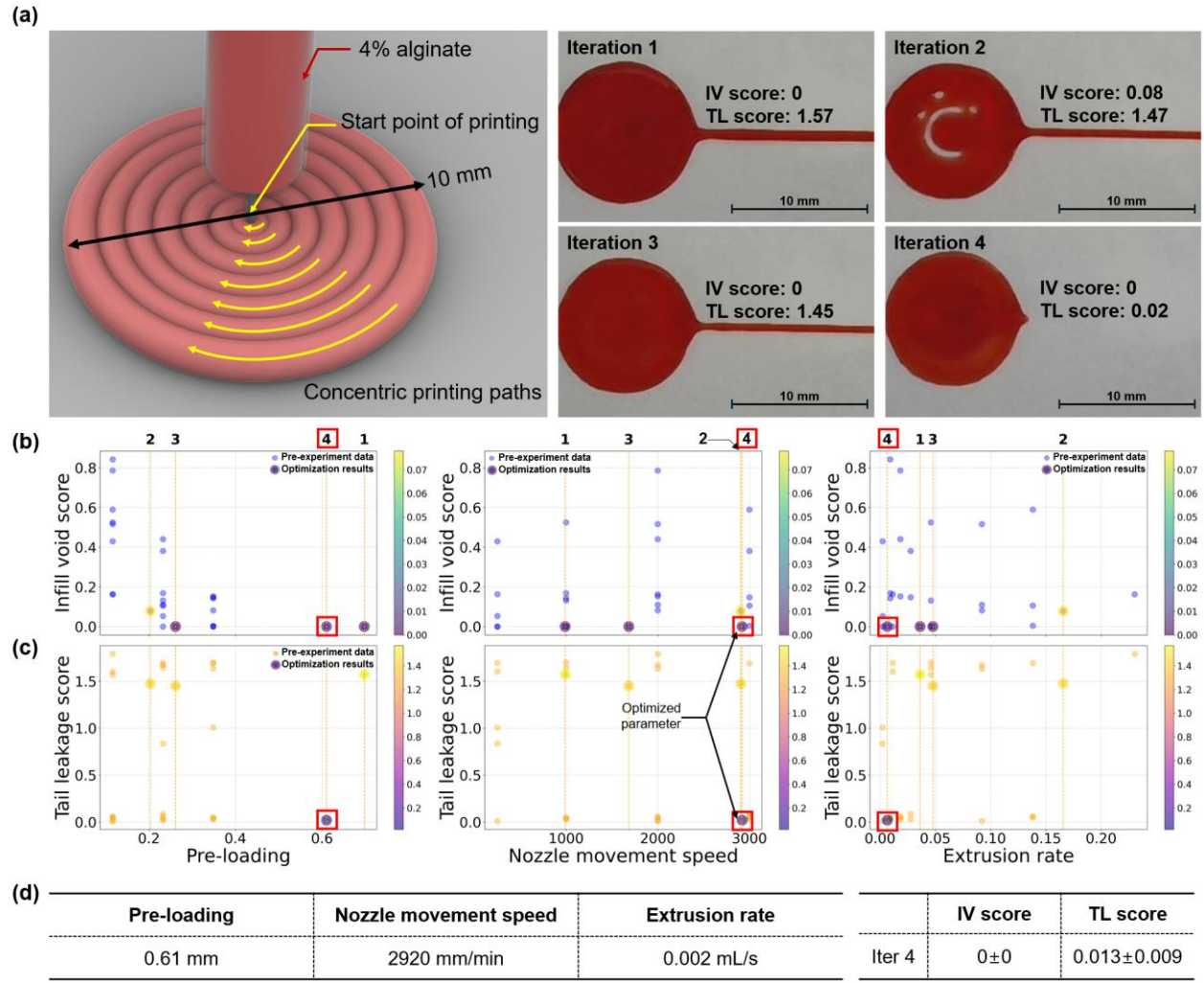


**Fig. 6** **a** Bayesian optimization process for circular shape with a 10 mm diameter using 4% alginate, **b** infill void and **c** tail leakage scores plotted against the pre-loading, nozzle movement speed, and extrusion rate. Square markers indicate the optimized parameter set achieved at Iteration 4, **d** optimization results

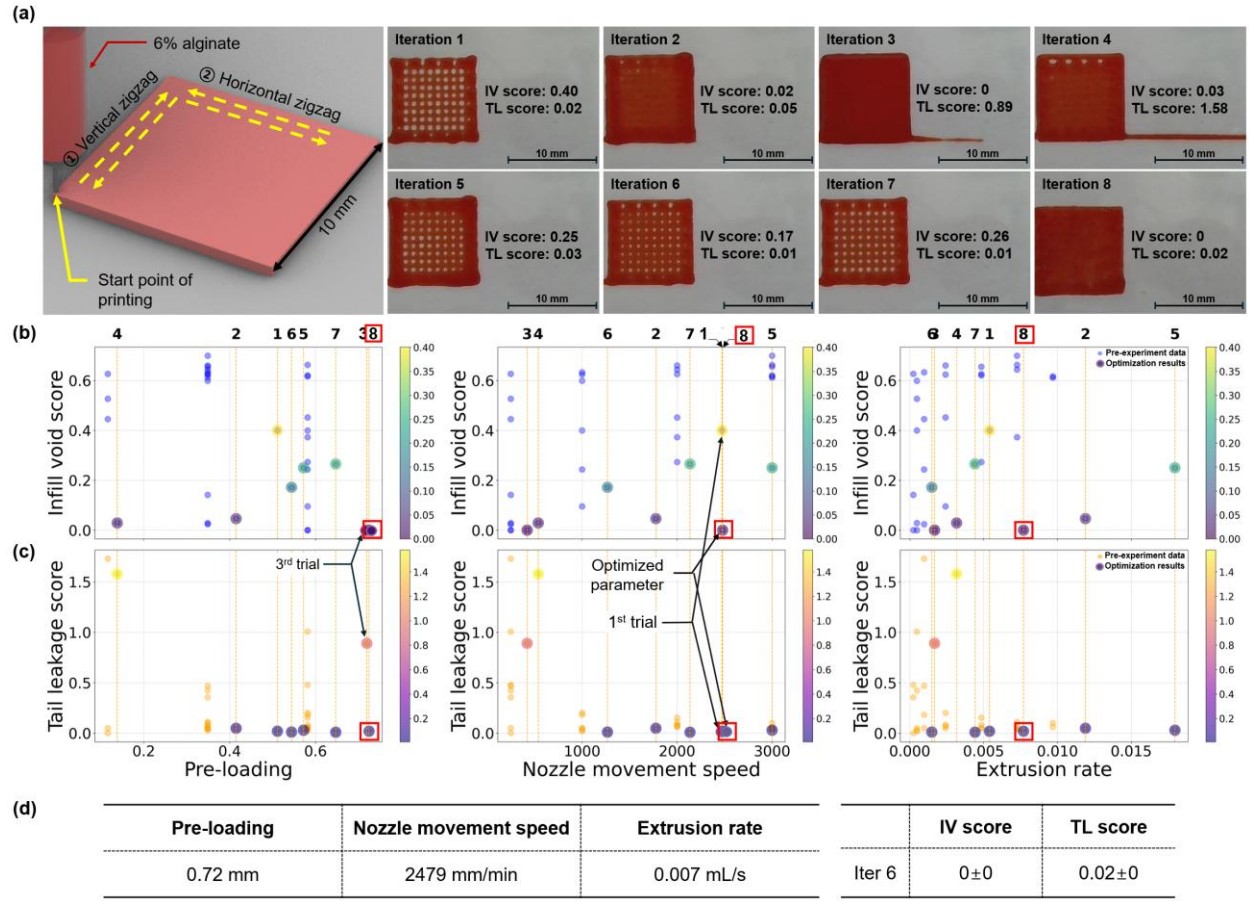


**Fig. 7** **a** Bayesian optimization process for 10×10 mm square with 6% alginate, **b** infill void and **c** tail leakage scores plotted against the pre-loading, nozzle movement speed, and extrusion rate. Square markers indicate the optimized parameter set achieved at Iteration 8, **d** optimization results

### Multilayering integration with Bayesian-optimized hydrogel printing

Maintaining structural integrity during the multilayering process is a major challenge in 3D printing, particularly for soft materials like hydrogels, which are prone to deformation and spreading after deposition (Bom et al., 2022). As previously discussed, we focused on optimizing in-plane printing to ensure layer-level stability, which is critical for building reliable hydrogel-based structures. This outcome was extended to 3D printing by applying the Bayesian-optimized parameters derived from 4% and 6% alginate prints, each with a layer height of approximately 1

mm, for multilayer fabrication (Fig. 8a). To ensure successful stacking, support sheets treated with calcium chloride were placed between layers to improve stacking stability and reduce spreading (Yoon et al., 2019). For 4% alginate, a layered structure with a height of approximately 7 mm was formed (Fig. 8b), while the higher viscosity of 6% alginate enabled the formation of additional layers, reaching 11 mm (Fig. 8c). The lower viscosity of 4% alginate led to more spreading and flattening after deposition, which made it difficult to maintain structural height. In contrast, the higher viscosity of 6% alginate better preserved the printed shape, allowing more layers to be stacked without collapse. These results reaffirm that increased viscosity facilitates more stable 3D hydrogel printing (Jang et al., 2018). However, the changes in viscosity necessarily require comprehensive tuning of printing parameters, which are closely interdependent. In this context, BO proves effective in achieving high shape fidelity of individual in-plane layers, which serve as the fundamental building blocks of 3D structures. Since 3D hydrogel printing inherently involves the accumulation of these unit layers, ensuring their quality is essential for achieving structural accuracy and robustness. This demonstrates the potential of BO not only as a tool for rapid parameter tuning but also as a foundation for enabling stable and precise 3D hydrogel architecture.

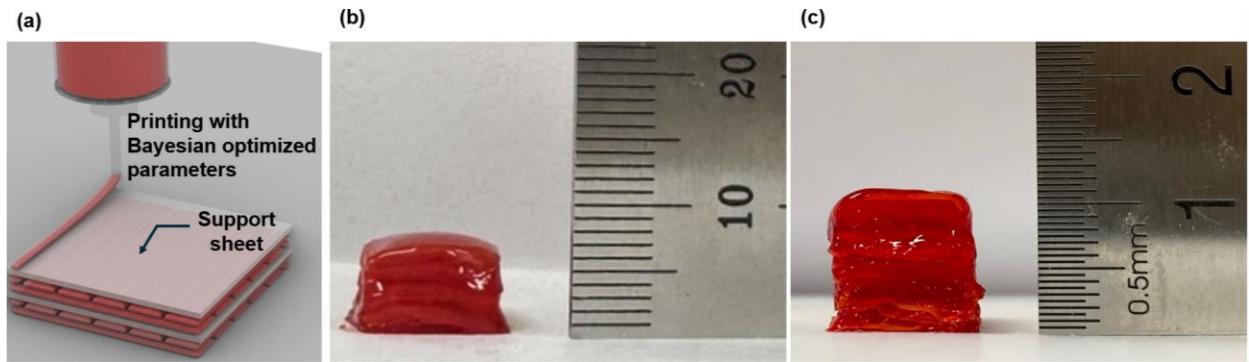


**Fig. 8** 3D multilayer hydrogel printing: **a** Schematic illustration of hydrogel printing on a support sheet for multilayering, **b** Printed structure with 6 layers of 4% alginate and **c** with 11 layers of 6% alginate



## Conclusion

This study proposed and validated a Bayesian optimization framework to improve print quality in extrusion-based 3D printing by optimizing three key parameters: pre-loading, nozzle movement speed, and extrusion rate. The framework builds an initial dataset, quantifies infill void and tail leakage, and models them with separate Gaussian Process Regression (GPR) models. These were combined into one objective function, enabling efficient simultaneous optimization in an automated loop. The framework was validated across different print sizes (10×10 and 20×20 squares), a different geometry (circular path), and varying alginate concentrations (4% and 6%), with optimal parameters identified after 6, 6, 8, 4 iterations, highlighting the minimal number of repetitions required, respectively. These results highlight the efficiency of the framework in adapting to diverse printing conditions. Although demonstrated with sodium alginate and basic geometries, the proposed optimization framework is not specific to a particular material or geometry. By defining appropriate process parameters, quality scores, and scoring methods for the new target, the same optimization flow can be applied to other bioinks with different rheological behaviors or to more complex geometries. Furthermore, the optimized in-plane parameters were successfully extended to 3D printing, confirming the feasibility of autonomous layer-by-layer deposition for hydrogel structures.

## References

- Amorim, P., d'Ávila, M., Anand, R., Moldenaers, P., Van Puyvelde, P., & Bloemen, V. (2021). Insights on shear rheology of inks for extrusion-based 3D bioprinting. *Bioprinting*, 22, e00129. <https://doi.org/10.1016/j.bprint.2021.e00129>
- Armstrong, A. A., Alleyne, A. G., & Johnson, A. J. W. (2020). 1D and 2D error assessment and correction for extrusion-based bioprinting using process sensing and control strategies. *Biofabrication*, 12(4), 045023. <https://doi.org/10.1088/1758-5090/aba8ee>
- Armstrong, A. A., Pfeil, A., Alleyne, A. G., & Johnson, A. J. W. (2021). Process monitoring and control strategies in extrusion-based bioprinting to fabricate spatially graded structures. *Bioprinting*, 21, e00126. <https://doi.org/10.1016/j.bprint.2020.e00126>
- Bom, S., Ribeiro, R., Ribeiro, H. M., Santos, C., & Marto, J. (2022). On the progress of hydrogel-based 3D printing: Correlating rheological properties with printing behaviour. *International Journal of Pharmaceutics*, 615, 121506. <https://doi.org/10.1016/j.ijpharm.2022.121506>
- Bourell, D., Kruth, J. P., Leu, M., Levy, G., Rosen, D., Beese, A. M., & Clare, A. (2017). Materials for additive manufacturing. *CIRP annals*, 66(2), 659-681. <https://doi.org/10.1016/j.cirp.2017.05.009>

- Chepiga, T., Zhilyaev, P., Ryabov, A., Simonov, A. P., Dubinin, O. N., Firsov, D. G., Kuzminova, Y. O., & Evlashin, S. A. (2023). Process parameter selection for production of stainless steel 316L using efficient multi-objective Bayesian optimization algorithm. *Materials*, 16(3), 1050. <https://doi.org/10.3390/ma16031050>
- Dharmadhikari, S., Menon, N., & Basak, A. (2023). A reinforcement learning approach for process parameter optimization in additive manufacturing. *Additive Manufacturing*, 71, 103556. <https://doi.org/10.1016/j.addma.2023.103556>
- Estelle, K. T., & Gozen, B. A. (2022). Complex ink flow mechanisms in micro-direct-ink-writing and their implications on flow rate control. *Additive Manufacturing*, 59, 103183. <https://doi.org/10.1016/j.addma.2022.103183>
- Franke, J., Heinrich, F., & Reisch, R. T. (2024). Vision based process monitoring in wire arc additive manufacturing (WAAM). *Journal of Intelligent Manufacturing*, 1-11. <https://doi.org/10.1007/s10845-023-02287-x>
- Frazier, P. I. (2018). A tutorial on Bayesian optimization. *arXiv preprint arXiv:1807.02811*. <https://doi.org/10.48550/arXiv.1807.02811>
- Gan, W., Ji, Z., & Liang, Y. (2021). Acquisition functions in Bayesian optimization. 2021 2nd International Conference on Big Data & Artificial Intelligence & Software Engineering (ICBASE),
- He, H., Zhu, Z., Zhang, Y., Zhang, Z., Famakinwa, T., & Yang, R. (2024). Machine condition monitoring for defect detection in fused deposition modelling process: a review. *The International Journal of Advanced Manufacturing Technology*, 1-30. <https://doi.org/10.1007/s00170-024-13630-8>
- He, K., Zhang, Q., & Hong, Y. (2019). Profile monitoring based quality control method for fused deposition modeling process. *Journal of Intelligent Manufacturing*, 30(2), 947-958. <https://doi.org/10.1007/s10845-018-1424-9>
- He, Y., Yang, F., Zhao, H., Gao, Q., Xia, B., & Fu, J. (2016). Research on the printability of hydrogels in 3D bioprinting. *Scientific reports*, 6(1), 29977. <https://doi.org/10.1038/srep29977>
- Huang, Y., Leu, M. C., Mazumder, J., & Donmez, A. (2015). Additive manufacturing: current state, future potential, gaps and needs, and recommendations. *Journal of Manufacturing Science and Engineering*, 137(1), 014001. <https://doi.org/10.1115/1.4028725>
- Jang, T.-S., Jung, H.-D., Pan, H. M., Han, W. T., Chen, S., & Song, J. (2018). 3D printing of hydrogel composite systems: Recent advances in technology for tissue engineering. *International Journal of Bioprinting*, 4(1), 126. <https://doi.org/10.18063/IJB.v4i1.126>
- Jiang, Z., Diggle, B., Tan, M. L., Viktorova, J., Bennett, C. W., & Connal, L. A. (2020). Extrusion 3D printing of polymeric materials with advanced properties. *Advanced Science*, 7(17), 2001379. <https://doi.org/10.1002/advs.202001379>
- Jin, Y., Chai, W., & Huang, Y. (2017). Printability study of hydrogel solution extrusion in nanoclay yield-



- stress bath during printing-then-gelation biofabrication. *Materials Science and Engineering: C*, 80, 313-325. <https://doi.org/10.1016/j.msec.2017.05.144>
- Jung, J., Park, K., Cho, B., Park, J., & Ryu, S. (2023). Optimization of injection molding process using multi-objective bayesian optimization and constrained generative inverse design networks. *Journal of Intelligent Manufacturing*, 34(8), 3623-3636. <https://doi.org/10.1007/s10845-022-02018-8>
- Kumar, S., Gopi, T., Harikeerthana, N., Gupta, M. K., Gaur, V., Krolczyk, G. M., & Wu, C. (2023). Machine learning techniques in additive manufacturing: a state of the art review on design, processes and production control. *Journal of Intelligent Manufacturing*, 34(1), 21-55. <https://doi.org/10.1007/s10845-022-02029-5>
- Lee, S.-M., & Park, S.-H. (2025). Autonomous in-situ defect detection and correction in additive-lathe 3D printing process using variational autoencoder model. *Additive Manufacturing*, 98, 104635. <https://doi.org/10.1016/j.addma.2024.104635>
- Li, J., Chen, M., Fan, X., & Zhou, H. (2016). Recent advances in bioprinting techniques: approaches, applications and future prospects. *Journal of translational medicine*, 14, 1-15. <https://doi.org/10.1186/s12967-016-1028-0>
- Liu, J., Ye, J., Momin, F., Zhang, X., & Li, A. (2022). Nonparametric Bayesian framework for material and process optimization with nanocomposite fused filament fabrication. *Additive Manufacturing*, 54, 102765. <https://doi.org/10.1016/j.addma.2022.102765>
- Lizotte, D. J. (2008). Practical bayesian optimization.
- Mantelli, A., Romani, A., Suriano, R., Levi, M., & Turri, S. (2021). Direct ink writing of recycled composites with complex shapes: process parameters and ink optimization. *Advanced Engineering Materials*, 23(9), 2100116. <https://doi.org/10.1002/adem.202100116>
- Munoz-Perez, E., Rubio-Retama, J., Cussó, L., Igartua, M., Hernandez, R. M., & Santos-Vizcaino, E. (2024). 3D-printed Laponite/Alginate hydrogel-based suppositories for versatile drug loading and release. *Drug Delivery and Translational Research*, 1-19. <https://doi.org/10.1007/s13346-023-01506-5>
- Naghieh, S., Sarker, M., Sharma, N., Barhoumi, Z., & Chen, X. (2019). Printability of 3D printed hydrogel scaffolds: Influence of hydrogel composition and printing parameters. *Applied Sciences*, 10(1), 292. <https://doi.org/10.3390/app10010292>
- Qin, Y., Qi, Q., Scott, P. J., & Jiang, X. (2019). Determination of optimal build orientation for additive manufacturing using Muirhead mean and prioritised average operators. *Journal of Intelligent Manufacturing*, 30, 3015-3034. <https://doi.org/10.1007/s10845-019-01497-6>
- Rau, D. A., Williams, C. B., & Bortner, M. J. (2023). Rheology and printability: A survey of critical relationships for direct ink write materials design. *Progress in Materials Science*, 101188.

- <https://doi.org/10.1016/j.pmatsci.2023.101188>
- Saadi, M., Maguire, A., Pottackal, N. T., Thakur, M. S. H., Ikram, M. M., Hart, A. J., Ajayan, P. M., & Rahman, M. M. (2022). Direct ink writing: a 3D printing technology for diverse materials. *Advanced Materials*, 34(28), 2108855. <https://doi.org/10.1002/adma.202108855>
- Saluja, A., Xie, J., & Fayazbakhsh, K. (2020). A closed-loop in-process warping detection system for fused filament fabrication using convolutional neural networks. *Journal of manufacturing processes*, 58, 407-415. <https://doi.org/10.1016/j.jmapro.2020.08.036>
- Shahriari, B., Swersky, K., Wang, Z., Adams, R. P., & De Freitas, N. (2015). Taking the human out of the loop: A review of Bayesian optimization. *Proceedings of the IEEE*, 104(1), 148-175. <https://doi.org/10.1109/JPROC.2015.2494218>
- Shevchik, S. A., Masinelli, G., Kenel, C., Leinenbach, C., & Wasmer, K. (2019). Deep learning for in situ and real-time quality monitoring in additive manufacturing using acoustic emission. *IEEE Transactions on Industrial Informatics*, 15(9), 5194-5203. <https://doi.org/10.1109/TII.2019.2910524>
- Siegel, J. E., Beemer, M. F., & Shepard, S. M. (2020). Automated non-destructive inspection of fused filament fabrication components using thermographic signal reconstruction. *Additive Manufacturing*, 31, 100923. <https://doi.org/10.1016/j.addma.2019.100923>
- Sridhar, S., Venkatesh, K., Revathy, G., Venkatesan, M., & Venkatraman, R. (2024). Adaptive fabrication of material extrusion-AM process using machine learning algorithms for print process optimization. *Journal of Intelligent Manufacturing*, 1-25. <https://doi.org/10.1007/s10845-024-02495-z>
- Umeda, T., Kozu, H., & Kobayashi, I. (2024). Analysis of pumpkin paste printability for screw-based 3D food printer. *Food and Bioprocess Technology*, 17(1), 188-204. <https://doi.org/10.1007/s11947-023-03116-y>
- Vaissier, B., Pernot, J.-P., Chougrani, L., & Véron, P. (2019). Genetic-algorithm based framework for lattice support structure optimization in additive manufacturing. *Computer-Aided Design*, 110, 11-23. <https://doi.org/10.1016/j.cad.2018.12.007>
- Webb, B., & Doyle, B. J. (2017). Parameter optimization for 3D bioprinting of hydrogels. *Bioprinting*, 8, 8-12. <https://doi.org/10.1016/j.bprint.2017.09.001>
- Whip, B., Sheridan, L., & Gockel, J. (2019). The effect of primary processing parameters on surface roughness in laser powder bed additive manufacturing. *The International Journal of Advanced Manufacturing Technology*, 103, 4411-4422. <https://doi.org/10.1007/s00170-019-03716-z>
- Wilson, A., & Adams, R. (2013). Gaussian process kernels for pattern discovery and extrapolation. *International conference on machine learning*,
- Yang, J., He, H., Li, D., Zhang, Q., Xu, L., & Ruan, C. (2023). Advanced strategies in the application of

gelatin-based bioink for extrusion bioprinting. *Bio-Design and Manufacturing*, 6(5), 586-608. <https://doi.org/10.1007/s42242-023-00236-4>

Zhang, Y., Apley, D. W., & Chen, W. (2020). Bayesian optimization for materials design with mixed quantitative and qualitative variables. *Scientific reports*, 10(1), 4924. <https://doi.org/10.1038/s41598-020-60652-9>

Zheng, Q., Xie, B., Xu, Z., & Wu, H. (2023). A systematic printability study of direct ink writing towards high-resolution rapid manufacturing. *International Journal of Extreme Manufacturing*, 5(3), 035002. <https://doi.org/10.1088/2631-7990/acd090>

## Appendix

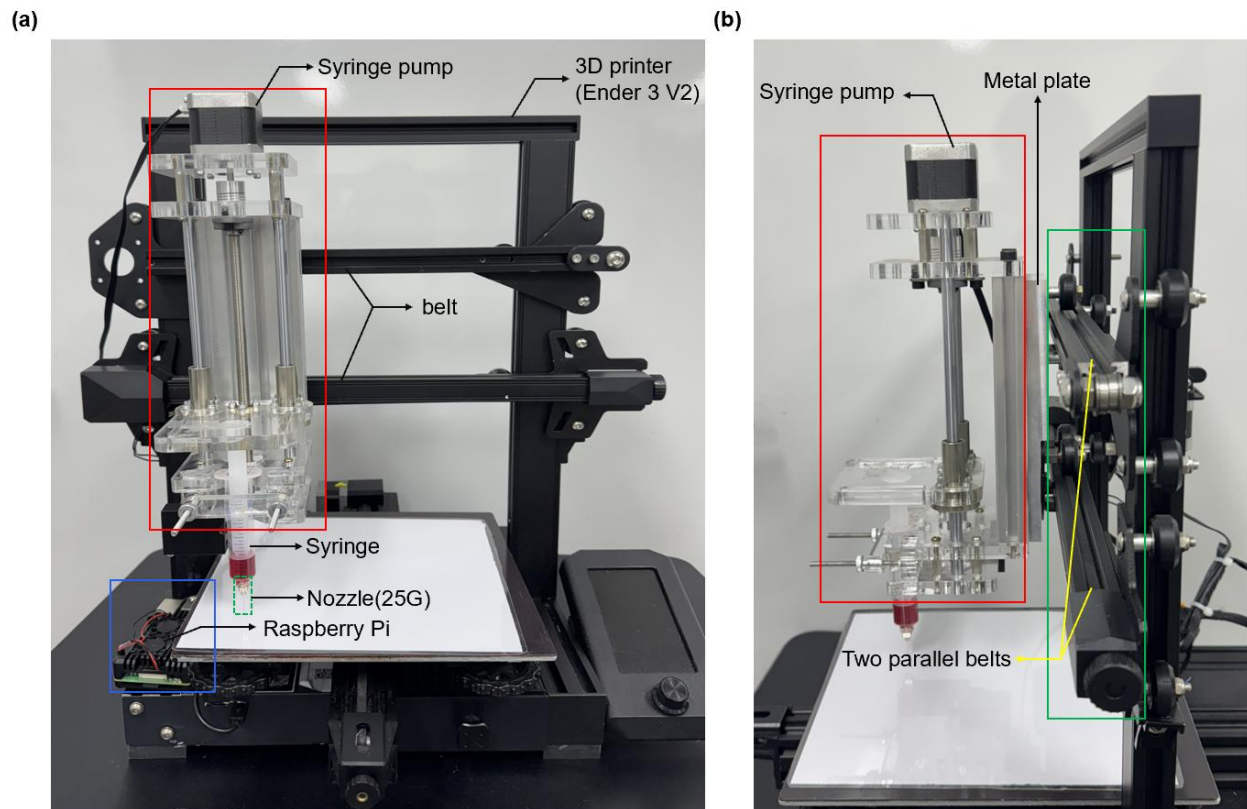


**Fig. 9** Extrusion-based 3D printing system, **a** front view of the system **b** side view of the system

	CLAHE	Threshold	Dilate iteration
Base	1.0	125	1
CLAHE high	1.5	125	1
CLAHE low	0.5	125	1
Threshold high	1.0	140	1
Threshold low	1.0	110	1
Dilate high	1.0	125	2
Dilate low	1.0	125	0

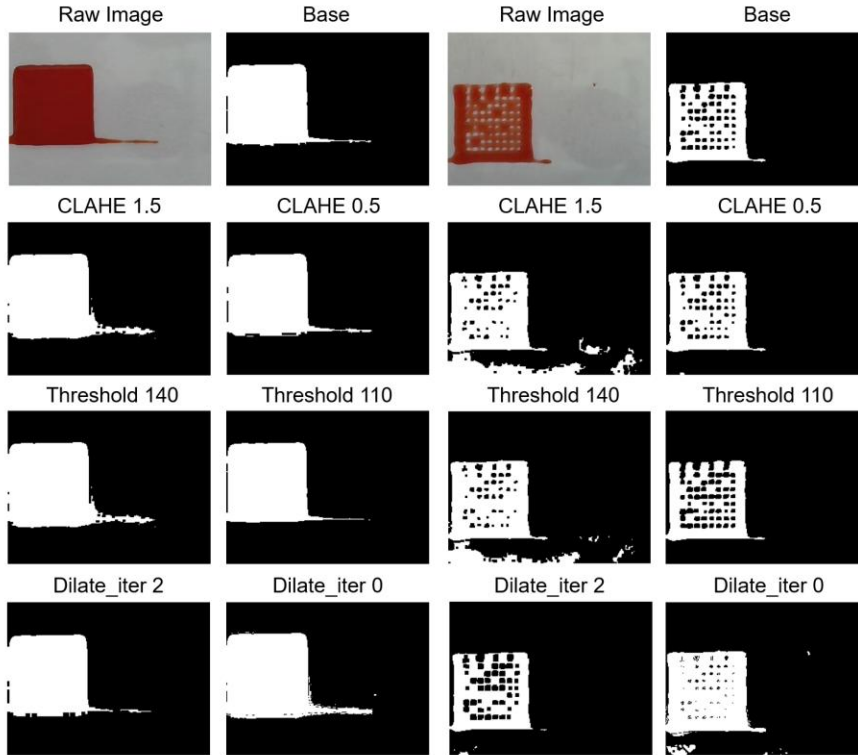


**Fig. 10** Effect of image processing parameters on defects of tail leakage and infill void

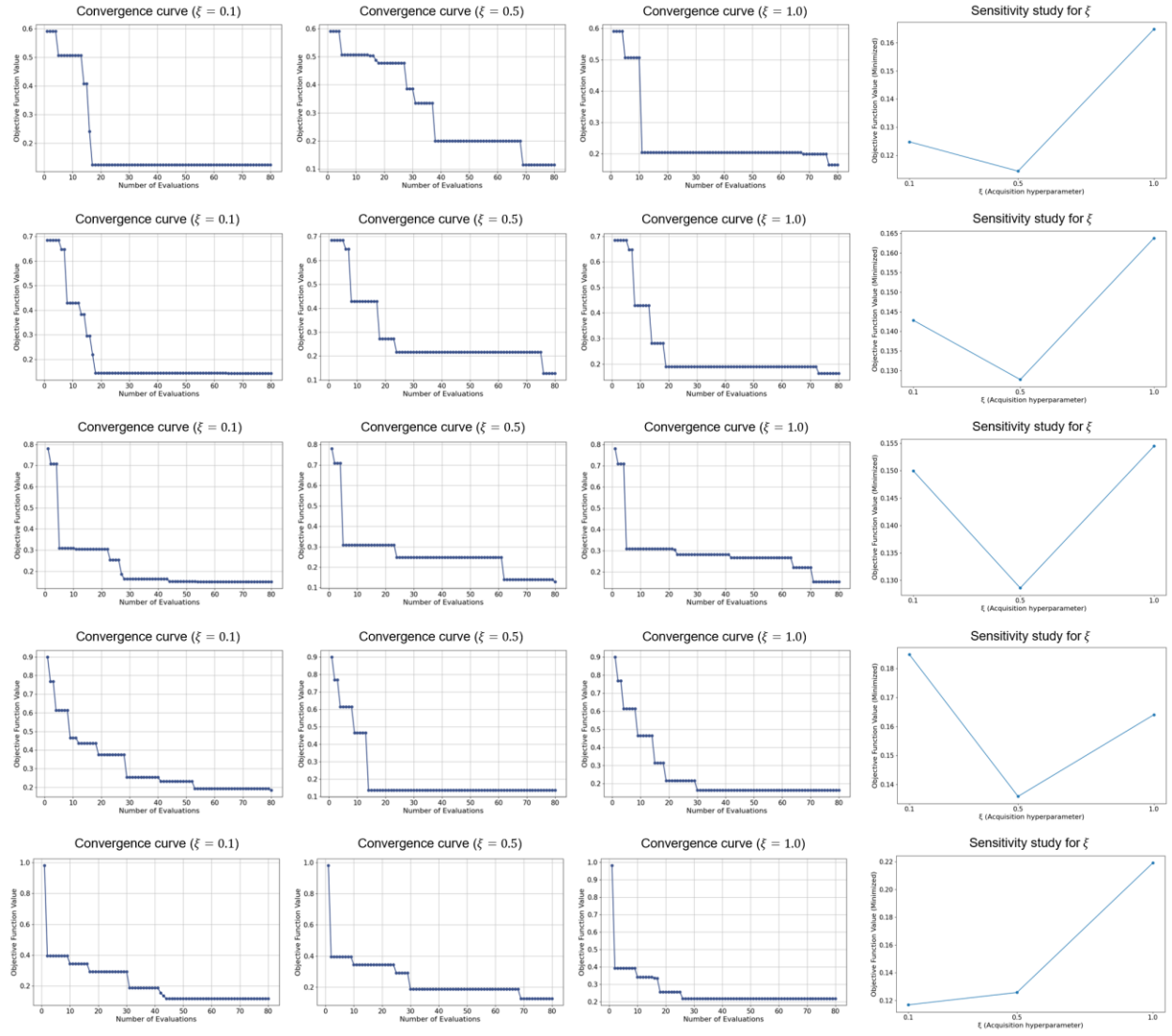
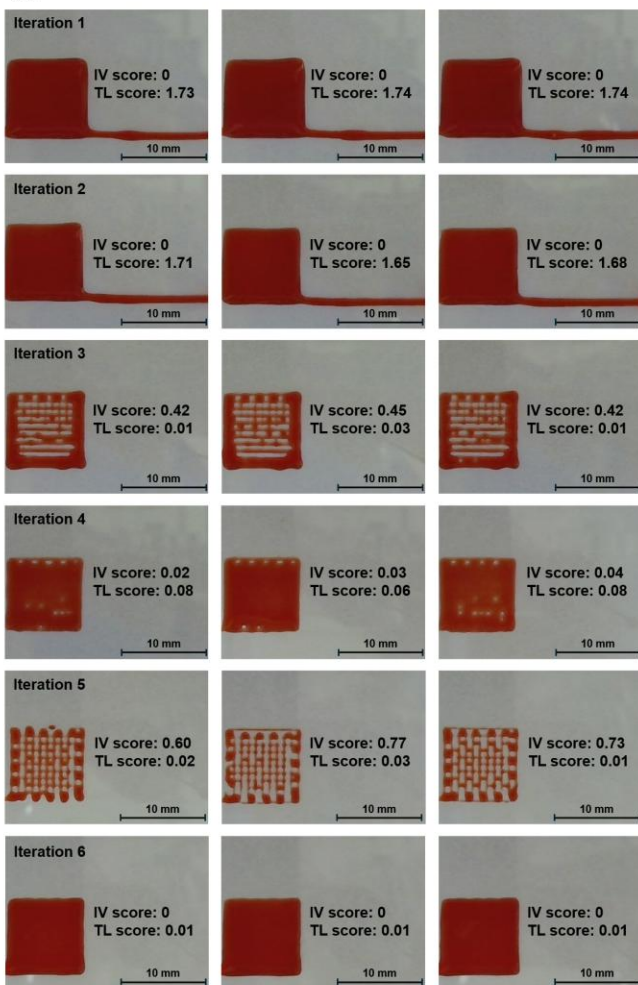


**Fig. 11** Convergence curves and sensitivity analysis for determining  $\xi$

(a)



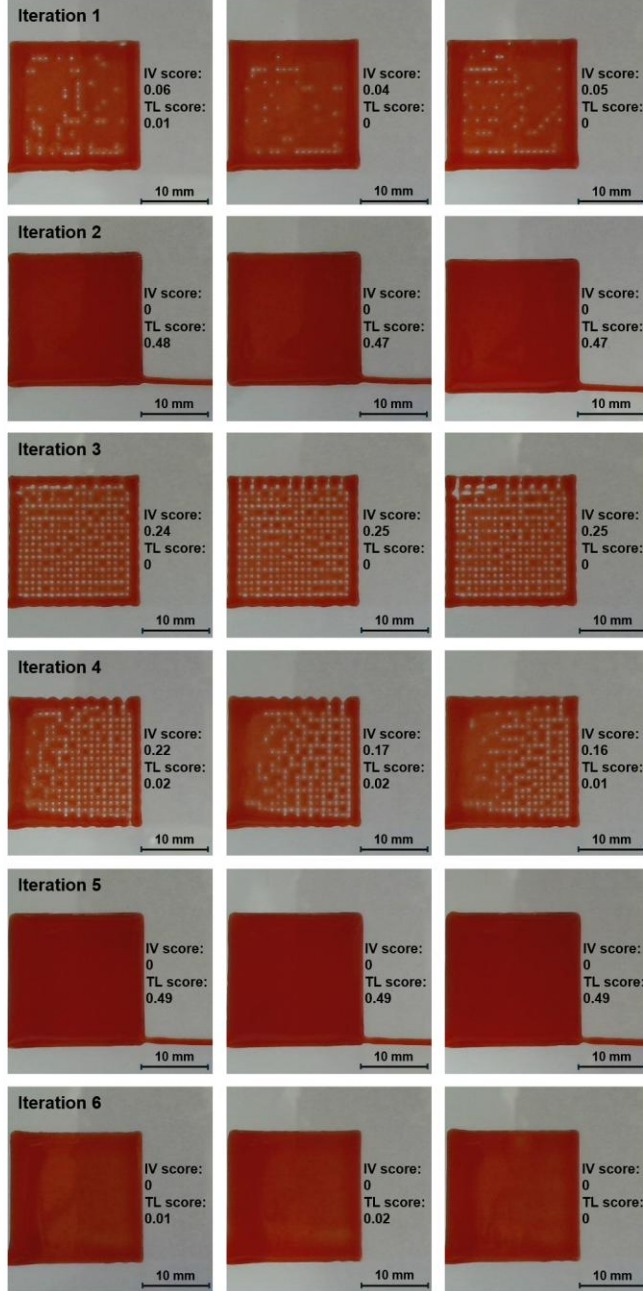
(b)

iter1	mean	std
IV score	0	0
TL score	1.74	0.0082
iter2	mean	std
IV score	0	0
TL score	1.685	0.0265
iter3	mean	std
IV score	0.4325	0.015
TL score	0.0275	0.0236
iter4	mean	std
IV score	0.0275	0.0096
TL score	0.0775	0.0126
iter5	mean	std
IV score	0.725	0.0881
TL score	0.0275	0.0171
iter6	mean	std
IV score	0	0
TL score	0.01	0

**Fig. 12** Bayesian optimization for 10×10 mm square with 4% alginate, **a** iterated printing results, **b** mean and standard deviation of IV and TL scores across iterations



(a)

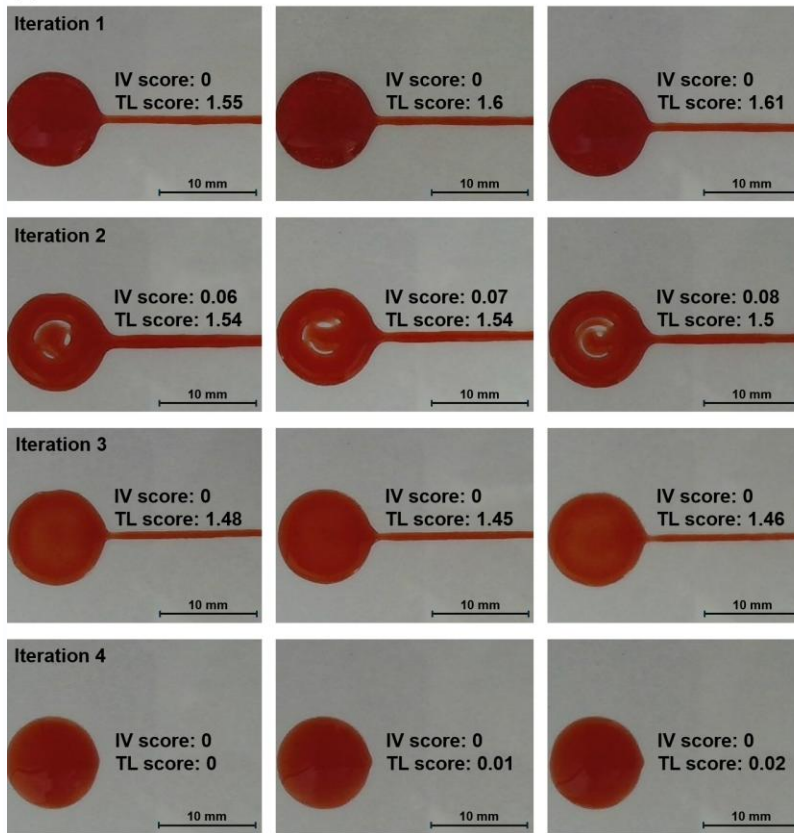


(b)

iter1	mean	std
IV score	0.05	0.0082
TL score	0.0025	0.005
iter2	mean	std
IV score	0	0
TL score	0.475	0.0058
iter3	mean	std
IV score	0.2475	0.005
TL score	0.0025	0.005
iter4	mean	std
IV score	0.1925	0.032
TL score	0.015	0.0058
iter5	mean	std
IV score	0	0
TL score	0.49	0
iter6	mean	std
IV score	0	0
TL score	0.01	0.008165

**Fig. 13** Bayesian optimization for 20×20 mm square with 4% alginate, **a** iterated printing results, **b** mean and standard deviation of IV and TL scores across iterations

(a)



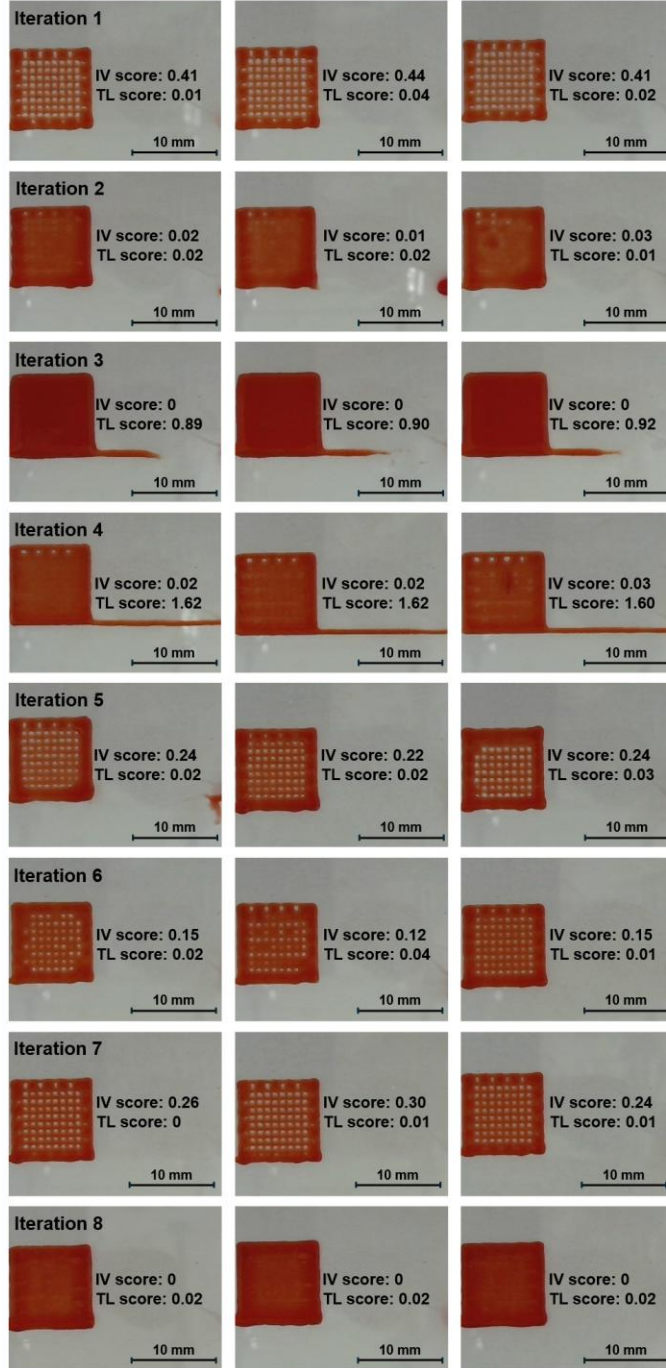
(b)

iter1	mean	std
IV score	0	0
TL score	1.5825	0.0275
iter2	mean	std
IV score	0.0725	0.0096
TL score	1.5125	0.034
iter3	mean	std
IV score	0	0
TL score	1.46	0.0141
iter4	mean	std
IV score	0	0
TL score	0.0125	0.00957

**Fig. 14** Bayesian optimization for circular shape with a 10 mm diameter using 4% alginate, **a** iterated printing results, **b** mean and standard deviation of IV and TL scores across iterations



(a)



(b)

iter1	mean	std
IV score	0.415	0.0173
TL score	0.0225	0.0126
iter2	mean	std
IV score	0.02	0.0082
TL score	0.05	0.025
iter3	mean	std
IV score	0	0
TL score	0.9	0.0141
iter4	mean	std
IV score	0.025	0.0058
TL score	1.605	0.0191
iter5	mean	std
IV score	0.2375	0.0126
TL score	0.025	0.0058
iter6	mean	std
IV score	0.1475	0.0126
TL score	0.02	0.0141
iter7	mean	std
IV score	0.265	0.0252
TL score	0.0075	0.005
iter8	mean	std
IV score	0	0
TL score	0.02	0

**Fig. 15** Bayesian optimization for 10×10 mm square with 6% alginate, **a** iterated printing results, **b** mean and standard deviation of IV and TL scores across iterations